Multigrid Methods for the 3D Simulation of Nonlinear Magneto-Mechanical Systems

M. Schinnerl, J. Schöberl
Special Research Program (SFB 013): Numerical and Symbolic Scientific Computing
Johannes Kepler University, A-4040 Linz, Austria

***Abstract*— A recently developed multigrid calculation scheme for coupled magneto-mechanical systems is presented. This scheme allows the efficient calculation of 3D dynamic rigid motions as well as deformations of anti-magnetic and ferromagnetic materials in a magnetic field. Thereby, the 3D mechanical problem is discretized with nodal elements and the 3D magnetic problem with edge elements. Both finite element meshes may be chosen independently and therefore, they can be adapted to the physical requirements of the mechanical and magnetic field. By applying fast multigrid solution techniques also for large scaled 3D problems very short solution times can be achieved. Computer simulations of three examples demonstrate the efficiency of the developed scheme.**

***Index Terms*— Multigrid methods, moving bodies, finite element methods, edge elements, eddy currents, magneto-mechanical systems**

I. Introduction

This paper deals with the numerical simulation of coupled magneto-mechanical systems, which are the basis of electro-magnetic transducers, such as sensors and actuators, magnetic bearings or electrical machines. In the past, the design of such systems have been based on time-consuming and therewith expensive empirical methods.
The precise numerical simulation of such coupled devices, which promises to improve this design process considerably, did not start longer ago than a couple of years. Reasons for this slow development of numerical techniques concerning these problems, are the difficult nonlinear coupling mechanisms between the mechanical and the magnetic field, and large requirements in respect to the computer hardware. In principle, the presently used numerical simulation techniques for magneto-mechanical systems can be subdivided into two classes. In the first case the whole system is calculated by using the finite-element-method (FEM). This strategy is used in [1] for the calculation of electric machines in the 2D case and is extended in [2] to 3D problems. The second method is based on coupling the FEM with the boundary-element-method (BEM), which reduces the number of unknowns and enables a simpler consideration of large mechanical displacements. This approach is applied in [3], and for more complex problems in [4] and [5].
The main disadvantage of these methods is the very large simulation time, which arises especially in the transient 3D case.
In this paper a numerical simulation technique, based on the FEM is presented, which is able to reduce the simulation times considerably. This is achieved by utilizing multigrid techniques [6] and different FEM-discretizations for the mechanical and the magnetic field. Thereby, it is possible to reduce the number of unknowns considerably, and to achieve "optimal complexity" of the numerical technique, which means, that the solution time increases only linear with the number of unknowns n.

M. Schinnerl, e-mail michael.schinnerl@jk.uni-linz.ac.at
This work has been supported by the Austrian Science Foundation - 'Fonds zur Förderung der wissenschaftlichen Forschung (FWF)' under project SFB F013 'Numerical and Symbolic Scientific Computing'

II. Theory of magneto-mechanical Systems

A. Mechanical System

If linear elasticity and isotropic linear material is assumed, the dynamical properties of the mechanical system can be described by

$$\frac{E}{2(1+\nu)}\left((\nabla\cdot\nabla)\vec{d}+\frac{1}{1-2\nu}\nabla(\nabla\cdot\vec{d})\right)+\vec{f}_V=\rho\frac{\partial^2\vec{d}}{\partial^2 t}+c\frac{\partial\vec{d}}{\partial t}. \tag{1}$$

At the boundary of the domain Ω_{mech} either the mechanical displacement $\vec{d}$ (Dirichlet boundary) or the mechanical stress $\vec{\sigma}$ (Neumann boundary) or a mechanical impedance is known [7]. In (1) $\vec{f}_V$ denotes the volume force, E the Young's modulus, ν the Poisson ratio, ρ the specific density and c a viscous damping of the material.

B. Magnetic System

If neglecting high frequent displacement currents, which can be done without restrictions for the considered class of problems, Maxwell's equations are

$$\nabla\times\vec{H} = \vec{J}, \tag{2}$$

$$\nabla\times\vec{E} = -\frac{\partial\vec{B}}{\partial t}, \tag{3}$$

$$\nabla \cdot \vec{B} = 0, \tag{4}$$

where $\vec{H}$ denotes the magnetic field strength, $\vec{J}$ the electric current density, $\vec{E}$ the electric field strength and $\vec{B}$ the magnetic induction. These equations are completed by the constitutive equations

$$\vec{B} = \mu\vec{H}, \tag{5}$$
$$\vec{J} = \vec{J}_e + \gamma\left(\vec{E} + \vec{v} \times \vec{B}\right), \tag{6}$$

where $\vec{v}$ is the velocity, γ the specific conductivity and μ the permeability of the material. $\vec{J}_e$ denotes a given current density. If surface currents are neglected, the conditions

$$\vec{n} \times \vec{H}_1 = \vec{n} \times \vec{H}_2, \tag{7}$$
$$\vec{n} \cdot \vec{B}_1 = \vec{n} \cdot \vec{B}_2, \tag{8}$$
$$\vec{n} \cdot \vec{J}_1 = \vec{n} \cdot \vec{J}_2, \tag{9}$$
$$\vec{n} \times \left(\vec{E}_1 + \vec{v}_1 \times \vec{B}_1\right) = \vec{n} \times \left(\vec{E}_2 + \vec{v}_2 \times \vec{B}_2\right), \tag{10}$$

must hold at an interface between two materials, specified by the indices 1 and 2. Thereby, $\vec{n}$ denotes the normal vector of the interface. By introducing the magnetic vector potential $\vec{A}$

$$\vec{B} = \nabla \times \vec{A} \tag{11}$$

and an electric scalar-potential Φ

$$\vec{E} = -\nabla\Phi - \frac{\partial \vec{A}}{\partial t}, \tag{12}$$

(2)-(6) can be transfered to

$$\nabla \times (\frac{1}{\mu}\nabla \times \vec{A}) + \gamma\frac{\partial \vec{A}}{\partial t} - \gamma\vec{v} \times (\nabla \times \vec{A}) = \vec{J}_e - \gamma\nabla\Phi. \tag{13}$$

For large Péclet-numbers

$$Pe = \frac{\mu\gamma v h}{2} >> 1 \tag{14}$$

the term $\gamma\vec{v} \times (\nabla \times \vec{A})$ becomes dominant and causes instabilities in the numerical solution process. In (14) h denotes the discretization parameter in direction of the velocity $\vec{v}$. An alternative possibility to consider the electromotive force is the formulation of the magnetic problem at the deformed geometry [8]. If observing a point P in a fixed reference frame $\Gamma(x, y, z)$ (Fig. 1), the spatial and temporal variation of the magnetic vector potential $\vec{A}$ at this point can be expressed by

$$\begin{aligned}\frac{\Delta\vec{A}}{\Delta t} &= \frac{\vec{A}(\vec{d} + \Delta\vec{d}, t + \Delta t) - \vec{A}(\vec{d}, t)}{\Delta t} \\ &= \frac{\vec{A}(\vec{d} + \Delta\vec{d}, t + \Delta t) - \vec{A}(\vec{d}, t + \Delta t)}{\Delta t} \\ &+ \frac{\vec{A}(\vec{d}, t + \Delta t) - \vec{A}(\vec{d}, t)}{\Delta t}.\end{aligned} \tag{15}$$

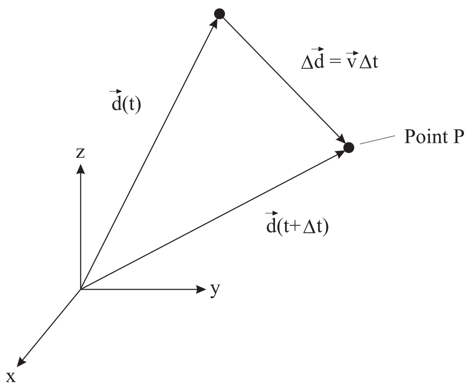

Fig. 1. Movement of a considered point P

In the limit $\Delta t \to 0$, (15) yields to

$$\frac{d\vec{A}}{dt} = \frac{\partial\vec{A}}{\partial t} + (\vec{v} \cdot \nabla)\vec{A}. \tag{16}$$

On the other hand, the electromotive force can be rewritten as

$$\vec{v} \times (\nabla \times \vec{A}) = \nabla_{\vec{A}}(\vec{v} \cdot \vec{A}) - (\vec{v} \cdot \nabla)\vec{A}. \tag{17}$$

Using (16) and (17) the partial differential equation (13) can be transformed into

$$\nabla \times (\frac{1}{\mu}\nabla \times \vec{A}) + \gamma\frac{d\vec{A}}{dt} - \gamma\nabla_{\vec{A}}(\vec{v} \cdot \vec{A}) = \vec{J}_e - \gamma\nabla\Phi. \tag{18}$$

Equation (18) illustrates, that the total differential $d\vec{A}/dt$ takes the electromotive force implicitly into account, but in return the term $\gamma\nabla_{\vec{A}}(\vec{v} \cdot \vec{A})$ must be considered additionally. If $\vec{v}$ and $\vec{A}$ are orthogonal, this term disappears, which is the case for all 2D problems. Besides the electromotive force, also magnetic forces cause a coupling between the magnetic and the mechanical field. The magnetic volume-force, produced by the magnetic field, can be separated into two parts. The first effect is the Lorentz-force,

$$\vec{f}_{V,L} = \vec{J} \times \vec{B}, \tag{19}$$

which accrues if a magnetic induction $\vec{B}$ acts at a body with a current-density $\vec{J}$. Using the magnetic vector potential $\vec{A}$, (19) can be rewritten as

$$\vec{f}_{V,L} = \left(\vec{J}_e - \gamma\nabla\Phi - \gamma\frac{dA}{dt} + \gamma\nabla_{\vec{A}}(\vec{v} \cdot \vec{A})\right) \times (\nabla \times \vec{A}). \tag{20}$$

In the case of non-constant permeability, especially in the presence of ferromagnetic materials, an additional force

$$\vec{f}_{V,\mu} = -\frac{1}{2}\left|\frac{1}{\mu}\nabla \times \vec{A}\right|^2 \nabla\mu \tag{21}$$

arises.

III. 3-D Finite Element Formulation

A. Mechanical System

By multiplying the mechanical differential equation (1) with a weighting function $\vec{w}$ and integrating over the domain Ω_{mech}, the mechanical problem is transferred to the weak form

$$\int_\Omega \vec{w} \cdot \left(\frac{E}{2(1+\nu)} \left((\nabla \cdot \nabla)\vec{d} + \frac{1}{1-2\nu} \nabla(\nabla \cdot \vec{d}) \right) + \vec{f}_V - c\frac{\partial \vec{d}}{\partial t} - \rho \frac{\partial^2 \vec{d}}{\partial^2 t} \right) d\Omega = 0. \quad (22)$$

Using Green's first identity one obtains [9]

$$\int_{\Omega_{mech}} w_i \rho \frac{\partial^2 d_i}{\partial t^2} d\Omega + \int_{\Omega_{mech}} \vec{\epsilon}(\vec{w})^T \mathbf{D} \vec{\epsilon}(\vec{d}) d\Omega + \int_{\Omega_{mech}} w_i c \frac{\partial d_i}{\partial t} d\Omega = \int_{\Omega_{mech}} w_i f_i d\Omega + \int_{\Gamma_{ni}} w_i \sigma_{ni} d\Gamma. \quad (23)$$

In (23) i denotes the spatial direction (x, y or z), $\vec{\epsilon}$ the mechanical strains, $\mathbf{D}$ the strain-stress relations and Γ_{ni} the boundary with given surface stress σ_{ni}. The mechanical domain is now discretized with nodal finite elements. Thereby, the mechanical displacement is approximated as

$$\vec{d} \approx \sum_{k=1}^{n_n} N_k \vec{d}_k. \quad (24)$$

N_k denotes the shape function of the k-th node, $\vec{d}_k$ the displacement at the k-th node and n_n the number of nodes. By using (24) in (23), and applying Galerkin's technique the ordinary second order differential-equation

$$\mathbf{M}\{\frac{\partial^2 d}{\partial t^2}\} + \mathbf{C}\{\frac{\partial d}{\partial t}\} + \mathbf{K}\{d\} = \{F\}, \quad (25)$$

is obtained. Thereby, the mass-matrix $\mathbf{M}$, the stiffness-matrix $\mathbf{K}$ and the force-vector $\{F\}$ have the form:

- mass-matrix:

$$\begin{aligned} \mathbf{M} &= [M_{ab}] \\ M_{ab} &= \delta_{ij} \int_\Omega N_a \rho N_b \, d\Omega \\ 1 \leq \; a,b \; &\leq n_{eq} \\ 1 \leq \; i,j \; &\leq n_{sd} \end{aligned} \quad (26)$$

- stiffness-matrix:

$$\begin{aligned} \mathbf{K} &= [K_{ab}] \\ K_{ab} &= \vec{e}_i^T \int_\Omega \mathbf{B}_a^T \mathbf{D} \mathbf{B}_b \, d\Omega \, \vec{e}_j \\ 1 \leq \; a,b \; &\leq n_{eq} \\ 1 \leq \; i,j \; &\leq n_{sd} \end{aligned} \quad (27)$$

in the 3D case:

$$\mathbf{B}_a = \begin{pmatrix} \frac{\partial N_a}{\partial x} & 0 & 0 \\ 0 & \frac{\partial N_a}{\partial y} & 0 \\ 0 & 0 & \frac{\partial N_a}{\partial z} \\ 0 & \frac{\partial N_a}{\partial z} & \frac{\partial N_a}{\partial y} \\ \frac{\partial N_a}{\partial z} & 0 & \frac{\partial N_a}{\partial x} \\ \frac{\partial N_a}{\partial y} & \frac{\partial N_a}{\partial x} & 0 \end{pmatrix} \quad (28)$$

- force-vector:

$$\begin{aligned} \{F\} &= \{F_a\} \\ F_a &= \int_\Omega N_a f_i d\Omega + \int_{\Gamma_{ni}} N_a \sigma_{ni} d\Gamma \end{aligned} \quad (29)$$

In (26) - (29) n_{eq} denotes the number of unknowns, $\vec{e}_i$ the unity vector in the spatial direction i, δ_{ij} Kronecker's operator and n_{sd} the spatial dimension of the mechanical field. The damping matrix $\mathbf{C}$ is chosen as a linear combination of $\mathbf{M}$ and $\mathbf{K}$ [10], i.e.

$$\mathbf{C} = \alpha \mathbf{M} + \beta \mathbf{K}. \quad (30)$$

The magnitudes of the Rayleigh coefficients α and β depend on the energy dissipation characteristics of the modeled mechanical problem.

B. Magnetic System

By multiplying the magnetic system (18) with a weighting function $\vec{W}$, integrating over the domain $\Omega_{mag}(\vec{d})$, which is deformed by the mechanical displacement $\vec{d}$, and applying the first Green's identity, the magnetic field can be expressed in a weak sense by

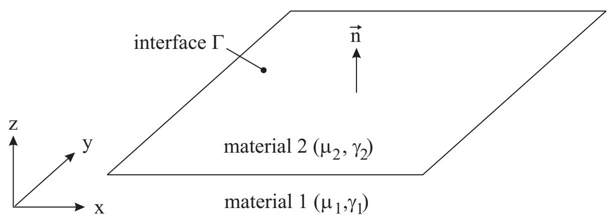

Fig. 2. Interface between two materials

$$\int_{\Omega_{mag}} \vec{W} \cdot \gamma \frac{dA}{dt} d\Omega + \int_{\Omega_{mag}} (\nabla \times \vec{W}) \cdot \frac{1}{\mu} (\nabla \times \vec{A}) \, d\Omega - \int_{\Omega_{mag}} \vec{W} \cdot \gamma \nabla_{\vec{A}} (\vec{v} \cdot \vec{A}) d\Omega = \int_{\Omega_{mag}} \vec{W} \vec{J}_e d\Omega - \int_{\Omega_{mag}} \gamma \vec{W} \cdot \nabla \Phi d\Omega + \int_{\Gamma_{mag,H}} \left(\vec{W} \cdot (\vec{H} \times \vec{n}) \right) d\Gamma. \quad (31)$$

In (31) $\Gamma_{mag,H}$ denotes a boundary with $\vec{H} \times \vec{n}$ specified. In order to achieve an appropriate FE-discretization of the magnetic system, the properties of the magnetic field at an interface must be analyzed in a more detailed way. In Fig. 2 an interface between two materials with the permeabilities μ_1 and μ_2 and the conductivities γ_1 and γ_2 is displayed. The interface lies in the x-y plane, therefore the normal-vector $\vec{n}$ is oriented exactly in z-direction. Using (11) and (8), the condition

$$B_n = B_z = \frac{\partial A_{y1}}{\partial x} - \frac{\partial A_{x1}}{\partial y} = \frac{\partial A_{y2}}{\partial x} - \frac{\partial A_{x2}}{\partial y} \tag{32}$$

must be fulfilled. Equation (32) can be enforced explicitly, if the tangential component of $\vec{A}$ is continuous at the interface. Since displacement currents are neglected, (9) can be expressed as

$$\vec{n} \cdot \gamma_1 \frac{\partial A_1}{\partial t} = \vec{n} \cdot \gamma_2 \frac{\partial A_2}{\partial t} \tag{33}$$

at a interface between two eddy current regions. Therefore, in z direction

$$\frac{\partial}{\partial t}[\gamma_1 A_{z1} - \gamma_2 A_{z2}] = 0 \tag{34}$$

must hold. As the magnetic vector potential is not static, (34) requires discontinuity of A_z if $\gamma_1 \neq \gamma_2$. The commonly used nodal elements enforce continuity of the tangential and normal component of $\vec{A}$. Therefore, nodal-elements violate (34) and they are only limited usable for the simulation of 3D eddy-current problems. Nevertheless it is possible to calculate 3D magnetic fields with nodal elements by using an additional potential ϕ [11], but in this formulation significant disadvantages of the nodal element discretization, like the bad approximation of $\vec{A}$ at interfaces, remain.
A more "natural" choice of the spatial discretization are edge-elements [12]. Thereby, the degrees of freedom are not asserted to the element nodes, but to the element edges. In Fig. 3 a linear edge-tetrahedron-element is

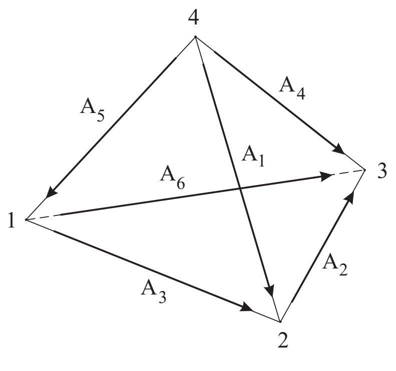

Fig. 3. linear edge-tetrahedron

shown. Using the edge element discretization, the magnetic vector field $\vec{A}$ is approximated by

$$\vec{A} \approx \int_{k=1}^{n_k} \vec{N}_k A_k. \tag{35}$$

In (35) $\vec{N}_k$ denotes the vectorial shape function, which is asserted to the k-th edge, n_k the number of edges in the magnetic FE mesh and

$$A_k = \int_k \vec{A} \cdot d\vec{s} \tag{36}$$

the line-integral over the projection of the magnetic vector potential $\vec{A}$ to the k-th edge. Inserting (35) into the weak formulation (31) leads to the ordinary first order differential equation system

$$\mathbf{L}\left\{\frac{\partial A}{\partial t}\right\} + \mathbf{P}\{A\} + \mathbf{P2}(\vec{v})\{A\} = \{Q\}. \tag{37}$$

The conductivity-matrix $\mathbf{L}$, the permeability-matrix $\mathbf{P}$, the second permeability matrix $\mathbf{P2}$ and the source vector $\{Q\}$ have the form:

- conductivity-matrix:

$$\begin{aligned} \mathbf{L} &= [L_{ab}] \\ L_{ab} &= \int_{\Omega_{mag}(\vec{d})} \vec{N}_a \cdot \gamma \vec{N}_b d\Omega \\ 1 \leq\ & a,b \leq n_k \end{aligned} \tag{38}$$

- permeability-matrix:

$$\begin{aligned} \mathbf{P} &= [P_{ab}] \\ P_{ab} &= \int_{\Omega_{mag}(\vec{d})} (\frac{1}{\mu}\nabla \times \vec{N}_a) \cdot (\nabla \times \vec{N}_b)\, d\Omega \\ 1 \leq\ & a,b \leq n_k \end{aligned} \tag{39}$$

- permeability-matrix 2:

$$\begin{aligned} \mathbf{P2} &= [P2_{ab}] \\ P2_{ab} &= -\int_{\Omega_{mag}(\vec{d})} \gamma \nabla_{\vec{A}}(\vec{v} \cdot \vec{N}_a) \cdot \vec{N}_b\, d\Omega \\ 1 \leq\ & a,b \leq n_k \end{aligned} \tag{40}$$

- source vector:

$$\begin{aligned} \{Q\} &= \{Q_b\} \\ Q_b &= \int_{\Omega_{mag}(\vec{d})} \vec{N}_a \cdot \gamma(\vec{J}_e - \nabla\phi)\, d\Omega \\ 1 \leq\ & b \leq n_k \end{aligned} \tag{41}$$

Thereby, the boundary integral term in (31) is assumed to be zero.

C. Voltage Clamping

Frequently the magnetic system (18) is not excited by a current density $\vec{J}_e$, but is coupled to an electrical network with a given voltage U. In Fig. 4 the simplest case of an electrical network, consisting of a resistor placed in series with the FE-model is shown. Thereby not only the magnetic vector potential $\vec{A}$, but also the current I is unknown. The network is described by

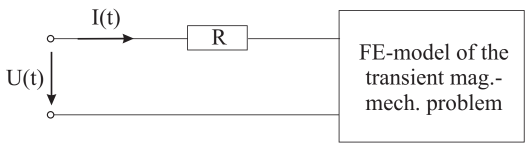

Fig. 4. External electrical network

$$U = RI + \frac{\partial \Psi}{\partial t}, \tag{42}$$

where the interlinkage flux is determined by

$$\Psi = \frac{n_c}{S_c} \int\limits_{\Omega_j} \vec{A} \cdot \vec{n}_s \, d\nu. \tag{43}$$

In (43) n_c denotes the number of turns of the coil in the FE model, S_c the crossectional area of the coil, $\vec{n}_s$ the unit tangential vector along the direction of the exciting current and Ω_j the region of the coil. On the other hand the current density $\vec{J}_e$ in the coil is described by

$$\vec{J}_e = \frac{n_c}{S_c} I \vec{n}_s. \tag{44}$$

Using (43) in (42) and (44) in (37) the coupled magnetic system can be written in the discrete form as

$$\mathbf{L}\{\frac{\partial A}{\partial t}\} \quad + \quad \mathbf{P}\{A\} + \mathbf{P2}(\vec{v})\{A\} = \mathbf{u}I, \tag{45}$$

$$RI \quad + \quad \mathbf{u}^T\{\frac{\partial A}{\partial t}\} = U. \tag{46}$$

Thereby, coupling vector $\mathbf{u}$ has the form

$$\mathbf{u} = \frac{n_c}{S_c} \int\limits_{\Omega_j} \vec{N}_i \cdot \vec{n}_s \, d\nu \ \in \ I\!R^{N_e \times 1}, \tag{47}$$

where N_e denotes the number of edges in the considered FE mesh.

IV. Iterative coupling procedure of the mechanical and magnetic field

A mathematical strong coupling of the mechanical and the magnetic system in one equation system is hard to realize, because the electromotive force is a non-linear term, i.e. both fields contribute directly to this effect. Additionally the Lorentz force and the interface force, caused by variations of the magnetic permeability, are quadratic functions of the magnetic vector potential $\vec{A}$. Therefore, an iterative coupling mechanism, used for instance in [13] and [5], is applied. Therewith, it is possible to consider variations of the magnetic field, which are caused by the mechanical displacement $\vec{d}$, easily. In order to achieve a good adaption of FE meshes to the mechanical and magnetic field, two different grids are used for both physical fields. Therefore, it is necessary to transfer data, like the mechanical displacement $\vec{d}$ or the magnetic volume-force $\vec{f}_V$, between the edge element discretization of the magnetic field and the nodal element discretization of the mechanical field. In section V. the projection mechanism for the mechanical and the magnetic mesh will be discussed in detail. The time discretization of the mechanical and the magnetic system is achieved by single time stepping algorithms.

A. Time Discretization of the Mechanical and the Magnetic System

The time discretization of the hyperbolic mechanical system (25) is performed by using Newmark's technique [9]. In order to achieve a shorter notation, the velocity at the nodes $\{\partial \vec{d}/\partial t\}$ is abbreviated by $\{v\}$ and the acceleration $\{\partial^2 d/\partial t^2\}$ is abbreviated by $\{a\}$. Additionally the curved brackets for the FE nodal and edge values are omitted. The index n denotes the variable at time $n\Delta t$, where Δt denotes the used time step. Applying Newmark's technique the requirements

$$\mathbf{M}a_{n+1} + \mathbf{C}v_{n+1} + \mathbf{K}d_{n+1} = F_{n+1}, \tag{48}$$

$$d_{n+1} = d_n + \Delta t v_n + \frac{\Delta t^2}{2}[(1-2\beta)a_n + 2\beta a_{n+1}], \tag{49}$$

$$v_{n+1} = v_n + \Delta t[(1-\gamma)a_n + \gamma a_{n+1}] \tag{50}$$

must be fulfilled. Thereby, β and γ denote parameters of Newmark's technique, which control the stability and accuracy of the method.
The parabolic magnetic system (37) is time discretized with a trapezidoal rule [9]. Thereby, the abbreviation R is used for the time derivation $\partial A/\partial t$ of the edge dofs. Applying the trapezidoal rule with the integration parameter α the following conditions must hold

$$\mathbf{L}R_{n+1} + \mathbf{P}A_{n+1} + \mathbf{P2}(\vec{v}_{n+1})A_{n+1} = Q_{n+1} \tag{51}$$

$$A_{n+1} = A_n + \Delta t R_{n+\alpha} \tag{52}$$

$$R_{n+\alpha} = (1-\alpha)R_n + \alpha R_{n+1}. \tag{53}$$

B. Iterative Coupling of the Mechanical and Magnetic System

The time discretization methods of the mechanical and magnetic system are coupled at each time step by an iterative technique:

- Step 1: Calculation of an approximation for the mechanical displacement and velocity at the mechanical mesh P_{mech}:

$$d_{n+1}^{app} = d_n + \Delta t v_n + \frac{\Delta t^2}{2} a_n \quad (54)$$
$$v_{n+1}^{app} = v_n + \Delta t a_n \quad (55)$$

- Step 2: Projection of d_{n+1}^{app} and v_{n+1}^{app} to the magnetic mesh
- Step 3: Distortion of the magnetic mesh by d_{n+1}^{app}. Reassembling of the conductivity-matrix $\mathbf{L}$ and the permeability matrix $\mathbf{P}$ at the deformed geometry. According to (16) the total differential of the magnetic vector potential is calculated by this updating, and thereby the electromotive force is implicitly taken into account. Additionally, the variation of the magnetic field, caused by the mechanical displacement, is considered by the updating process.
- Step 4: Calculation of the magnetic system:
  - The matrix $\mathbf{P2}(\vec{v})$ is non-symmetric and depends on the velocity $\vec{v}$, therefore, this term is only approximated by a predictor value.
    Approximations:

$$A_{n+1}^{app} = A_n + \Delta t R_n, \quad (56)$$
$$\mathbf{P2}(v_{n+1}) A_{n+1} = \mathbf{P2}(v_{n+1}^{app}) A_{n+1}^{app}. \quad (57)$$

  - Equation:

$$\mathbf{L}^* R_{n+1} = Q_{n+1} - \mathbf{P} A_n - (1-\alpha)\Delta t \mathbf{P} R_n - \mathbf{P2}(v_{n+1}^{app}) A_{n+1}^{app} \quad (58)$$
$$\mathbf{L}^* = \mathbf{L} + \alpha \Delta t \mathbf{P} \quad (59)$$

  - Corrector:

$$A_{n+1} = A_n + (1-\alpha)\Delta t R_n + \alpha \Delta t R_{n+1} \quad (60)$$

- Step 5: Calculation of the magnetic induction $\vec{B}$ and the magnetic forces $\vec{f}_V$
- Step 6: Projection of $\vec{f}_V$ to the mechanical FE mesh
- Step 7: Calculation of the mechanical field:
  - Predictor:

$$\tilde{d}_{n+1} = d_n + \Delta t v_n + \frac{\Delta t^2}{2}(1-2\beta) a_n \quad (61)$$
$$\tilde{v}_{n+1} = v_n + (1-\gamma)\Delta t a_n \quad (62)$$

  - Equation:

$$\mathbf{M}^* a_{n+1} = F_{n+1} - \mathbf{C}\tilde{v}_{n+1} - \mathbf{K}\tilde{d}_{n+1} \quad (63)$$
$$\mathbf{M}^* = \mathbf{M} + \gamma \Delta t \mathbf{C} + \beta \Delta t^2 \mathbf{K} \quad (64)$$

  - Corrector:

$$d_{n+1} = \tilde{d}_{n+1} + \beta \Delta t^2 a_{n+1} \quad (65)$$
$$v_{n+1} = \tilde{v}_{n+1} + \gamma \Delta t a_{n+1} \quad (66)$$

- Step 8: If no convergence reached, back to step 3
- Step 9: Calculate next time step

For practical problems only a very low number of iterations per time steps is necessary.

C. *Calculation of the magnetic field in the presence of ferromagnetic materials*

Ferromagnetic materials have a non-constant magnetic permeability μ. Thereby, the condition

$$\vec{H} = \frac{1}{\mu(\vec{B})}\vec{B}. \quad (67)$$

holds. It is assumed, that the material is isotropic, i.e. that μ is equal in each direction, and that no hysteresis effects arise. In the nonlinear case (58) has the form

$$\mathbf{L}^*(A) R_{n+1} = Q_{n+1} - \mathbf{P}(A) A_n - (1-\alpha)\Delta t \mathbf{P}(A) R_n - \mathbf{P2}(v_{n+1}^{app}) A_{n+1}^{app}. \quad (68)$$

In (68) the modified conductivity-matrix $\mathbf{L}^*$ and the permeability-matrix $\mathbf{P}$ depend on the edge degrees of freedom. The nonlinear magnetic field is calculated by a fixpoint method [14], which is described by the following algorithm:

- Step 1: Calculation of an initial guess A_{n+1}^i by using the variables of the time step n

$$i = 0 \quad (69)$$
$$A_{n+1}^i = A_n + \Delta t R_n \quad (70)$$
$$R_{n+1}^i = 0 \quad (71)$$

- Step 2: Reassembling of the matrices $\mathbf{L}^*$ and $\mathbf{P}$
- Step 3: Calculation of improved guesses R_{n+1}^{i+1} and A_{n+1}^{i+1}.

$$\mathbf{L}^*(A_{n+1}^i) R_{n+1}^{i+1} = Q_{n+1} - \mathbf{P}(A_{n+1}^i) A_n - (1-\alpha)\Delta t \mathbf{P}(A_{n+1}^i) R_n - \mathbf{P2}(v_{n+1}^A) A_{n+1}^i \quad (72)$$
$$A_{n+1}^{i+1} = A_n + (1-\alpha)\Delta t R_n + \alpha \Delta t R_{n+1}^{i+1} \quad (73)$$

- Step 4: Convergence test:
  - If:

$$\frac{\|R\|_{n+1}^{i+1} - \|R\|_{n+1}^i}{\|R\|_{n+1}^i} \geq \epsilon \quad (74)$$

    $i = i + 1$, back to Step 2

- Else:
  Calculation of the next time step

In many cases this algorithm is oscillating or only slowly convergent, but the method can be stabilized by a line-search algorithm [14]. Thereby step 3 of the iteration is modified:

- Step 3.1: Calculation of improved guesses R^i_{n+1} and A^i_{n+1}
- Step 3.2: Calculation of a search direction

$$\delta R_{n+1} = R^{i+1}_{n+1} - R^i_{n+1} \quad (75)$$

$$\delta A_{n+1} = A^{i+1}_{n+1} - A^i_{n+1} \quad (76)$$

- Step 3.3: Choosing of a relaxation parameter τ and calculation of modified guesses

$$R^\tau_{n+1} = R^i_{n+1} + \tau \delta R_{n+1} \quad (77)$$

$$A^\tau_{n+1} = A^i_{n+1} + \tau \delta A_{n+1} \quad (78)$$

- Step 3.4: Reassembling of $\mathbf{L}^*$ and $\mathbf{P}$ and calculation of the residuum $\Psi(\tau)$ and the projection of the residuum to the search direction $G(\tau)$

$$\begin{aligned} \Psi(\tau) &= \mathbf{L}^* R^\tau_{n+1} - Q_{n+1} \\ &+ \mathbf{P} A^\tau_{n+1} + \mathbf{P2}(v^{app}_{n+1}) A^{app}_{n+1} \end{aligned} \quad (79)$$

$$G(\tau) = \delta R_{n+1} \cdot \Psi(\tau) \quad (80)$$

The relaxation parameter τ is now chosen in such a way, that the projection of the residuum to the search direction is a minimum. Since even for strong nonlinear materials $G(\tau)$ is approximately a linear function of τ, it is sufficient to calculate $G(\tau)$ for two different values of τ and to determine the optimal τ with linear interpolation. This method leads to a fast convergent and very stable solution process with comparatively low numerical effort.

D. Modifications in the Case of Voltage Clamping

One possibility to consider the external network is the coupling of (45) and (46) in one matrix equation system [13]. Thereby, the structure of the arising system matrix is destroyed, which may lead to a slower convergence of the used iterative MG solvers. Therefore, in this paper an alternative strong coupling method of the magnetic field and the network is chosen, which preserves the structure of the system matrix. By multiplying (45) with the inverse modified mass-matrix $\mathbf{L}^{*,-1}$, for the time discretized case the expression

$$\begin{aligned} R_{n+1} = \mathbf{L}^{*,-1}\mathbf{u} I_{n+1} - \mathbf{L}^{*,-1}\big[\mathbf{P} A_n \\ -(1-\alpha)\Delta t \mathbf{P} R_n - \mathbf{P2}(v^{app}_{n+1}) A^{app}_{n+1}\big] \end{aligned} \quad (81)$$

can be achieved. If using the abbreviation

$$\tilde{A}_{n+1} = \mathbf{P} A_n - (1-\alpha)\Delta t \mathbf{P} R_n - \mathbf{P2}(v^{app}_{n+1}) A^{app}_{n+1} \quad (82)$$

and inserting (81) in the time discretized form of (46) the relation

$$U_{n+1} = \mathbf{u}^T \mathbf{L}^{*,-1} \mathbf{u} I_{n+1} + R\, I_{n+1} - \mathbf{u}^T \mathbf{L}^{*,-1} \tilde{A}_{n+1}, \quad (83)$$

which can be rewritten as

$$I_{n+1} = \frac{U_{n+1} + \mathbf{u}^T \mathbf{L}^{*,-1} \tilde{A}_{n+1}}{\mathbf{u}^T \mathbf{L}^{*,-1} \mathbf{u} + R}, \quad (84)$$

is obtained. Therefore, in the case of voltage clamping the calculation of the magnetic field at each time step is modified:

- Approximations:

$$A^{app}_{n+1} = A_n + \Delta t R_n, \quad (85)$$

$$\mathbf{P2}(v_{n+1}) A_{n+1} = \mathbf{P2}(v^{app}_{n+1}) A^{app}_{n+1}. \quad (86)$$

- Equation:

$$\begin{aligned} \tilde{A}_{n+1} = \mathbf{P} A_n - (1-\alpha)\Delta t \mathbf{P} R_n \\ - \mathbf{P2}(v^{app}_{n+1}) A^{app}_{n+1} \end{aligned} \quad (87)$$

$$I_{n+1} = \frac{U_{n+1} + \mathbf{u}^T \mathbf{L}^{*,-1} \tilde{A}}{\mathbf{u}^T \mathbf{L}^{*,-1} \mathbf{u} + R} \quad (88)$$

$$R_{n+1} = \mathbf{L}^{*,-1}\mathbf{u} I^{n+1} - \mathbf{L}^{*,-1} \tilde{A} \quad (89)$$

- Corrector:

$$A_{n+1} = A_n + (1-\alpha)\Delta t R_n + \alpha \Delta t R_{n+1} \quad (90)$$

The terms $\mathbf{L}^{*,-1}\mathbf{u}$ and $\mathbf{L}^{*,-1}\tilde{A}$ of (89) are already known from (88) and it is not necessary to calculate them again. Additionally, in the linear case the term $\mathbf{L}^{*,-1}\mathbf{u}$ is constant and must be calculated only for the first time step. Therefore, only the equation system

$$\mathbf{L}^* \xi = \tilde{A}, \quad (91)$$

has to be solved at each iteration step.
Also in the case of voltage clamping, for non-linear problems the line-search algorithm presented in subsection C is applied to (88) and (89).

V. Multigrid Methods

Applying the presented FE technique to 3D coupled fields may lead to long simulation times. These long times are caused by

- a high number of unknowns,
- large bandwidth of the FE matrices,
- calculation of many time steps,
- and iteration loops at each time step.

Thereby, the main time consuming part of the in section IV. presented algorithm is the solution of the matrix equation systems (58) and (63) at each iteration loop. Using multigrid techniques the solution times for this equation systems can be reduced considerably.

A. Multigrid solver for the mechanical system

1) Generation of a hierarchy of FE-spaces: In contrast to standard FE techniques the multigrid method is not based on a fixed FE mesh, which describes the unknown field variable accurate enough. Using multigrid techniques first a very coarse discretization T_1 of the field problem is chosen. Then the elements of T_1 are dissected and thereby a finer discretization T_2 is generated. In Fig. 5 the dissection of one tetrahedron element of T_1 into 8 tetrahedron elements of T_2 is shown. This refinement process can include either all elements (uniform refinement) or only a part of the elements (adaptive refinement). The dissection of the mesh is repeated, until a discretization T_l is obtained, which is able to describe the mechanical field accurate enough. By this repeated refinement a hierarchy of FE discretizations $T_1, ..., T_l$ is generated, and for each of the FE meshes T_q, $q = 1, 2, ..., l$ the equation system (63), which is abbreviated as

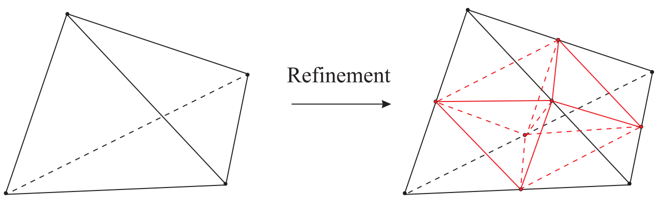

Fig. 5. Refinement of a tetrahedron element

$$\mathbf{A}_q x_q = f_q \tag{92}$$

can be assembled. Additionally, an interpolation operator I_q^{q+1} is defined, which transfers an arbitrary FE nodal function ξ_q at level q into an equivalent nodal function ξ_{q+1} at level $q+1$. With I_q^{q+1} the condition

$$\xi_{q+1} = I_q^{q+1} \xi_q \tag{93}$$

holds. Vice versa the restriction of the right hand side to the coarser grid q is given by

$$f_q = I_{q+1}^q f_{q+1}, \tag{94}$$

whereby I_{q+1}^q denotes the restriction operator. At each level q smoothing operators G_q are defined, which must be adapted to the mechanical problem. Using the components I_q^{q+1}, I_{q+1}^q and G_q the classical two-grid algorithm, as the simplest exponent of the multigrid methods, can be defined.

2) Classical two-grid algorithm: $x_{q,j,s}$ denotes the approximation of the solution x at the level q, the current multigrid iteration j and the status of the current iteration s. In the two-grid method the multigrid hierarchy consists only of one coarse grid $q-1$ and one finer grid q.

Given: Approximation $x_{q,j}$ after j two-grid iterations

1. ν_1 smoothing operations at the finest level q
$$x_{q,j,1} = (G_q)^{\nu_1} x_{q,j} \tag{95}$$
2. Calculation of the defect
$$d_q = f_q - \mathbf{A}_q x_{q,j,1} \tag{96}$$
and restriction of the defect to the coarse grid
$$d_{q-1} = I_q^{q-1} d_q. \tag{97}$$
3. Solution of the coarse grid system
$$\mathbf{A}_{q-1} w_{q-1} = d_{q-1}. \tag{98}$$
4. Prolongation of w_{q-1} to the finer grid
$$w_q = I_{q-1}^q w_{q-1} \tag{99}$$
and correction of the smoothed approximation $x_{q,j,1}$
$$x_{q,j,2} = x_{q,j,1} + w_q. \tag{100}$$
5. ν_2 smoothing operations at the level q
$$x_{q,j,3} = (G_q)^{\nu_2} x_{q,j,2} \tag{101}$$

MG iteration stop: $x_{q,j+1} = x_{q,j,3}$

The presented two-grid algorithm leads to very good approximations of x after a small number of iterations [15]. Thereby, at each two-grid iteration only $\nu_1 + \nu_2$ smoothing iteration sweeps and a direct solution at the level $q-1$ must be performed. Nevertheless, in many cases the solution process of (98) at the coarser grid $q-1$ is too time and memory consuming. In order to avoid this difficulty the two-grid algorithm is recursively restarted for (98). Repeating this process for all available grids a MG V-cycle is generated, which is displayed in Fig. 6. Thereby, at

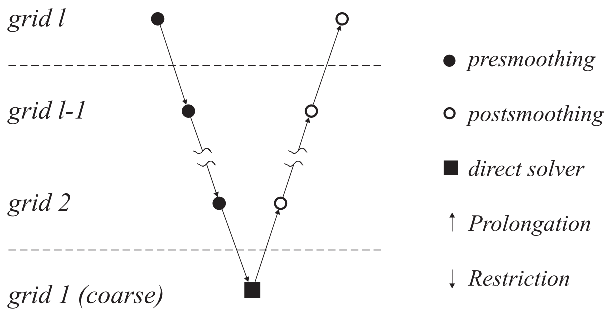

Fig. 6. MG solution algorithm (V-Cycle)

each level only smoothing operations are necessary, and at the coarsest grid $q = 1$ a linear equation system of the form $\mathbf{A}_1 w_1 = d_1$ must be solved with a conventional direct or iterative solver. Since at this grid the number of unknowns is generally low, this solution process is not very time and memory consuming. Additionally, it can be shown, that MG methods have "optimal complexity", that means, that the number of necessary arithmetical operations and the memory consumption increase only linear with the number of unknowns at the finest level l [6].

3) Choosing the grid transfer operators: The interpolation operator I_q^{q+1} is obtained by using the FE shape functions. Thereby, in the case of a linear discretization the value $\vec{x}_{q+1}^i$ of an arbitrary node i at the level $q+1$ can be determined by

$$\vec{x}_{q+1}^i = \begin{cases} \vec{x}_q^i & \text{if the node } i \\ & \text{is part of level } q \\ 0.5(\vec{x}_q^{i1} + \vec{x}_q^{i2}) & \text{if } i \text{ is in the center} \\ & \text{of an edge between the} \\ & \text{nodes } i_1 \text{ and } i_2 \end{cases} \tag{102}$$

The restriction operator I_{q+1}^q is chosen to be the transposed to I_q^{q+1}, i.e.

$$I_{q+1}^q = (I_q^{q+1})^T. \tag{103}$$

4) Smoothing operators: Multigrid methods use at each level smoothers, which damp strongly oscillating errors. Operators of the Gauss-Seidel type [16] are especially suitable for this purpose. In the case of a 3D elasticity problem, the displacements d_x, d_y and d_z of a node i couple very strongly. Therefore, they are combined in a vector $\{x\}_i$ and a Block-Gauss-Seidel smoothing technique [17] is used. To analyze the situation in more detail the matrices $\mathbf{A}$ at the different grid levels are rewritten as

$$\mathbf{A} = \begin{bmatrix} \mathbf{D}_1 & \mathbf{A}_{1,2} & \dots & \mathbf{A}_{1,n} \\ \mathbf{A}_{2,1} & \mathbf{D}_2 & \dots & \mathbf{A}_{2,n} \\ \vdots & & & \\ \mathbf{A}_{n,1} & \mathbf{A}_{n,2} & \dots & \mathbf{D}_n \end{bmatrix}, \tag{104}$$

whereby the displacement of the i-th node is determined by

$$\begin{aligned} &\mathbf{A}_{i,1}\{x\}_1 + \dots + \mathbf{A}_{i,i-1}\{x\}_{i-1} + \mathbf{D}_i\{x\}_i \\ &+\mathbf{A}_{i,i+1}\{x\}_{i+1} + \dots + \mathbf{A}_{i,n}\{x\}_n = \{f\}_i. \end{aligned} \tag{105}$$

The matrices $A_{i,j}$ and D_i are blocks of the dimension 3×3 and $\{f\}_i$ is the right hand side at the node i. By using a given approximation $\{x\}_i^k$ of the displacement in the node i, a smoothed approximation $\{x\}_i^{k+1}$ is determined by

$$\begin{aligned} \mathbf{D}_i\{x\}_i^{k+1} = \sum_{j=1}^{i-1}(-\mathbf{A}_{i,j})\{x\}_j^{k+1} + \sum_{j=i+1}^{n}(-\mathbf{A}_{i,j})\{x\}_j^k \\ +\{f\}_i. \end{aligned} \tag{106}$$

5) MG as preconditioner of the conjugate gradient method (CG): The convergence and robustness of the solution process can be further improved, by using the MG method as preconditioner of standard iterative methods, like CG [16]. Thereby the solution of a symmetric, positive definite linear matrix equation system $\mathbf{A}x = f$ is obtained by the following algorithm:

1. Start:
   Initial guess x^0;
   $$d^0 = f - \mathbf{A}x^0;\ \zeta_a = 1;\ g^0 = 0;$$
2. Iteration ($k = 1, 2, 3, \dots$):
   $$\begin{aligned} \mathbf{C}_{pre}\rho^{k-1} &= d^{k-1} \qquad (107) \\ \zeta &= \zeta^{k-1}\cdot\rho^{k-1};\ \tilde{e}_{k-1} = \zeta/\zeta_a \\ g^k &= -\rho^{k-1} + \tilde{e}_{k-1}g^{k-1} \\ z &= \mathbf{A}g^k \\ \tilde{q}_k &= \zeta/(g^k\cdot z);\ \zeta_a = \zeta; \\ x^k &= x^{k-1} + \tilde{q}_k g^k;\ r^k = r^{k-1} + \tilde{q}_k z; \end{aligned}$$
3. Test convergence

$\mathbf{C}_{pre}$ denotes the precondition matrix. Using MG in the preconditioned conjugate gradient method, (107) is solved by the presented MG techniques. In [6] this method is analyzed in a more detailed way.

B. Multigrid solver for the magnetic problem

Since the magnetic vector potential $\vec{A}$ is discontinuous at material interfaces the magnetic problem is discretized by edge elements. Therefore, a straight forward application of multigrid methods to 3D magnetic fields is not possible and an alternative approach presented in [18] and [19] is used.

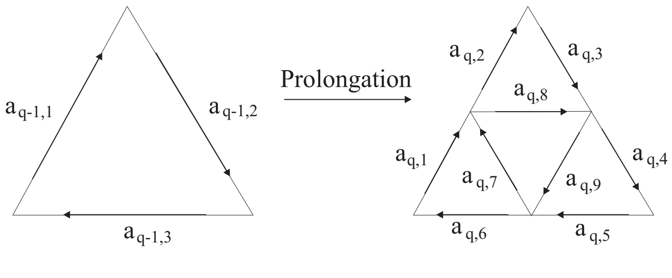

Fig. 7. Prolongation of the edge degrees of freedom from level $q-1$ to level q

1) Choosing the grid transfer operators: In order to determine the grid transfer operators between the levels $q-1$ and q, the refinement of a face F^{q-1} of an edge tetrahedron element on the level $q-1$ is analyzed. By dissecting the tetrahedron at the level $q-1$ into 8 tetrahedrons at the level q, the area of F^{q-1} is replaced by 4 new faces $F_1^q, .., F_4^q$ (Fig. 7). A suitable prolongation I_{q-1}^q

must guarantee that the magnetic flux Φ across F^{q-1} and $F_1^q + .. + F_4^q$ is equal, i.e. the condition

$$\int\limits_{F^{q-1}} (\nabla \times \vec{A}) \cdot d\vec{F} = \sum_{k=1}^{4} \int\limits_{F_k^q} (\nabla \times \vec{A}) \cdot d\vec{F} \qquad (108)$$

must hold. Using Stoke's law, (108) can be rewritten as the integral over the edges

$$\oint\limits_{\partial F^{q-1}} \vec{A} \cdot d\vec{s} = \sum_{k=1}^{4} \oint\limits_{\partial F_k^q} \vec{A} \cdot d\vec{s}, \qquad (109)$$

or, by exploiting the degrees of freedom of the FE formulation (Fig. 7), as

$$\begin{aligned} a_{q-1,1} + a_{q-1,2} + a_{q-1,3} &= a_{q,1} - a_{q,7} + a_{q,6} + a_{q,2} \\ +a_{q,3} - a_{q,8} + a_{q,4} + a_{q,5} &- a_{q,9} + a_{q,7} + a_{q,8} + a_{q,9}. \end{aligned} \qquad (110)$$

The transfer operator

$$I_{q-1}^q = \begin{pmatrix} .5 & .5 & 0 & 0 & 0 & 0 & -.25 & -.25 & .25 \\ 0 & 0 & .5 & .5 & 0 & 0 & .25 & -.25 & -.25 \\ 0 & 0 & 0 & 0 & .5 & .5 & -.25 & .25 & -.25 \end{pmatrix}^T$$

fulfills the requirements of the flux conservation, which can be proofed by inserting I_{q-1}^q into (110) and in the corresponding conditions for the single faces F_1^q - F_4^q. The restriction operator I_q^{q-1} is chosen to be the transposed to I_{q-1}^q, i.e.

$$I_q^{q-1} = (I_{q-1}^q)^T. \qquad (111)$$

2) Smoothing operators: The task of the smoothers in the multigrid cycle is to damp out strongly oscillating errors. A simple Gauss-Seidel method does not behave well for Maxwell problems, but due to [19] and [18] it is known, that properly designed block - Gauss-Seidel iterations do the job. Each block is assigned to a vertex of the mesh and connects all edges sharing this node. Since the edges of the magnetic mesh are asserted to more then one node, no standard block-Gauss-Seidel smoother but a overlapping technique must be applied. Thereby, for each of the N_V vertices V_k a connectivity matrix

$$\mathbf{R}_k = \begin{pmatrix} 1 & \dots & 0 & 0 & 0 & \dots \\ 0 & \dots & 0 & 1 & 0 & \dots \\ \dots & \dots & & & & \end{pmatrix}$$

is specified, which has the number of edges on the current node V_k rows and N_e columns. Using this matrix, we can pick out the quadratic sub-blocks $\mathbf{P_k}$ of the matrix $\mathbf{P}$ by

$$\mathbf{P}_k = \mathbf{R}_k \mathbf{P} \mathbf{R}_k^T. \qquad (112)$$

Each of these small matrices have to be inverted in the preparation phase of the multigrid method. One step of the block Gauss-Seidel iteration with initial approximation $a_{j,0} = a_j$ is defined as

$$a_{j,k+1} = a_{j,k} + \mathbf{R}_k^T \mathbf{P}_k^{-1} \mathbf{R}_k (f - \mathbf{P} a_{j,k}), \qquad k = 1, \dots N_V. \qquad (113)$$

It has to be mentioned, that not the whole residual $f - \mathbf{P}a_{j,k}$ has to be computed at each step, but only the few components picked out which R_k. Therefore, one block Gauss-Seidel step is not much more expensive than a simple Gauss-Seidel step.

VI. TEAM-Workshop problem 20

In order to demonstrate the advantages of the presented scheme, three examples are analyzed. First the TEAM Workshop problem 20 is considered. With this pure magnetic problem the convergence behavior of the multigrid solvers is compared to standard approaches. The second example, which will be discussed in the next section, is a nonlinear magnetic circuit which is coupled to an voltage clamped external circuit. Thereby the numerical computation is verified with the analytical solution of the corresponding nonlinear network of the coupled problem. The third example is a coupled magneto-mechanical system which is geometrically nonlinear. Thereby, different grids for the mechanical and magnetic field are used. Again the MG solution process is compared with standard techniques.

The TEAM Workshop problem 20 is a 3D, nonlinear and static magnetic field problem [20]. The structure of this problem, consisting of a center pole, a yoke and a coil, is displayed in Fig. 8. The coil is loaded with 4 different ex-

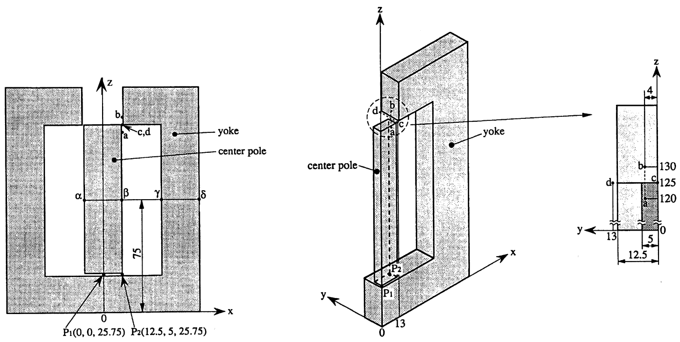

Fig. 8. Principal setup of TEAM-Workshop problem 20

citation currents, which cause a strong saturation in the ferromagnetic center pole and yoke.

A. Nested Multigrid

This nonlinear problem is calculated by using the iteration technique presented in section IV. First the structure is discretized with a coarse mesh T_1 of linear edge tetrahedron-elements, which is shown in Fig. 9. Thereby, the symmetries of the problem in the x-z plane and the y-z plane are exploited. By dissecting each edge tetrahedron element of the level 1 into 8 elements of the level 2, a new refined mesh T_2 is obtained. This procedure is repeated until a mesh T_4 is produced which is accurate enough to

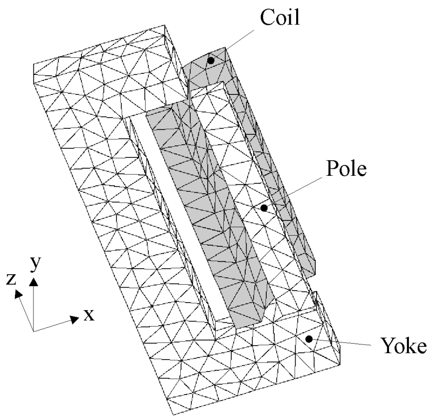

Fig. 9. Coarse FE discretization of TEAM problem 20 (without air)

describe the magnetic field. In Table I the generated hierarchy of FE meshes is shown. In order to achieve a

TABLE I
FE hierarchy of TEAM problem #20

grid level	edge elements	edges (dofs)
1	3050	3800
2	24500	30500
3	196000	236000
4	1570000	1900000

good initial guess for the nonlinear iteration procedure at the finer levels, the problem is first solved at the coarser grids and the solution is prolongated to the finer meshes and used as a start approximation for the nonlinear iteration process. By this "nested" multigrid approach the number of costly iterations at the finer grids is reduced considerably [21].

B. Simulation times

1) Convergence of the MG-PCCG solver: The most time consuming part of the computation process is the solution of the matrix equation system (68) at the finest mesh T_4. Thereby, the MG solver is compared to a standard solution technique, based on a CG method with adapted block preconditioning (PCCG). In Fig. 10 the convergence behavior of both methods for a matrix equation system at the finest level with 1900000 edges is displayed. The MG solver achieves the requested normalized residual of 10^{-6} after 13 iterations and 890 s, whereas the conventional iterative solver needs 180 iterations and 9860 s. Thereby, a SGI ORIGIN with RS12000 processor (300 MHz) is used. If applying a conventional CG solver with incomplete Cholesky preconditioning (ICCG) to the matrix equation (68) more than 1000 iterations would be necessary and therefore much higher simulation times arise [22].

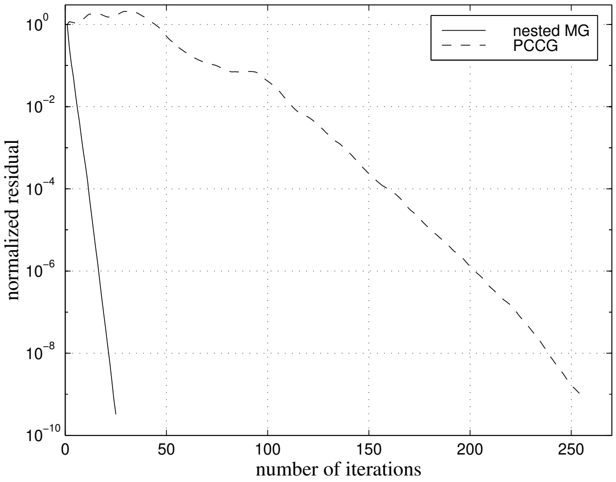

Fig. 10. Number of iterations versus normalized residual

2) Optimal complexity: To show the optimal complexity of the MG solver, the number of necessary iterations and the solution time to achieve a normalized residuum of 10^{-6} at each discretization level are displayed in Table II. Since the number of MG iterations is almost independent

TABLE II
Necessary MG-PCCG iterations and simulation times to reduce the normalized residuum of a matrix equation system to 10^{-6}

Level	iterations	time(s)
1	10	1.5
2	12	11
3	12	105
4	13	890

of the size of the FE meshes and the time for a single MG iteration increases linearly with the number of unknowns, a linear dependency between the degrees of freedom and the solution time can be detected.

3) Accumulated solution times of nested MG and a conventional approach: In Table III the convergence behavior of the nonlinear iterations process is compared for different excitations Θ. For small Θ the number of necessary iterations at the coarser levels is low, but if the excitation increases, a higher number of iterations is necessary. On the other hand due to the nested MG approach the number of iterations on the finer levels is almost independent of the strength of the nonlinearity. Since the iterations on the finer grids are the most time consuming parts of the computation process, also the accumulated simulation time is almost independent from the strength of the magnetic nonlinearity. In the 7-th column of Table III the accumulated simulation time of a conventional approach, that means PCCG solvers for the arising matrix equation systems and without exploiting the coarse grid information at the finer grids, is displayed. Thereby, a considerable advantage of the nested MG technique can

TABLE III
Necessary nonlinear iterations for different excitations Θ
Computer: SGI ORIGIN, RS12000 processor 300 MHz

Θ	iterat. at level				accum. time	accum. time
(AT)	1	2	3	4	nested MG (s)	conventional (s)
1000	4	3	3	2	8300	45400
3000	11	6	5	3	9570	114500
4500	15	6	5	3	9600	154000
5000	17	6	5	3	9600	173600

be detected.

C. Comparison measurement - simulation

In [20] the measured magnetic induction $\vec{B}$ at different points and the measured electromagnetic force $\vec{f}_{mag}$ to the center pole are given. These results are compared to the simulation results obtained at the finest mesh with 1900000 degrees of freedom. In Table IV the average flux densities B_z in the center pole (α-β) and the yoke (γ-δ) are displayed. Thereby, a very good agreement between measurement and simulation is achieved. At next the flux densities B_z are compared (Table V) at the points P_1 and P_2. At P_1 the numerical result agrees very well with the measurements, whereas at P_2, which is situated at the interface between the pole and air, slight differences arise, because at this point a very strong gradient of the magnetic flux can be detected. Another critical test for the numerical simulation is the calculation of the magnetic force, which acts to the center pole, since the force calculation is very sensitive to variations of the magnetic field. If the magnetic flux $\vec{B}$ and the magnetic field strength $\vec{H}$ at the surface of the center pole are known, the magnetic force $\vec{f}_{mag}$ can be calculated by integrating Maxwell's stress tensor [23]

$$\vec{T} = (\vec{n}\vec{H})\vec{B} - \vec{n}\frac{1}{2}\vec{B}\vec{H} \tag{114}$$

over the boundary Γ_{pole} of the pole, i.e.

$$\vec{f}_{mag} = \int_{\Gamma_{pole}} \vec{T}\, d\vec{\Gamma}. \tag{115}$$

In (114) $\vec{n}$ denotes the normal vector of the surface Γ_{pole} pointing away from the center pole. Table VI compares the z-component of the calculated magnetic force to the measurements. Thereby, for all excitations, a good agreement is achieved.

TABLE IV
Average z-component of the magnetic flux

$\Theta(A)$	$B_z(\alpha-\beta)$ (T)		$B_z(\gamma-\delta)$ (T)	
	sim.	meas.	sim.	meas.
1000	0.71	0.72	0.13	0.13
3000	1.78	1.75	0.36	0.36
4500	2.02	2.01	0.44	0.43
5000	2.04	2.05	0.45	0.46

TABLE V
Magnetic flux in the points P_1 and P_2

$\Theta(A)$	$B_z(P_1)$ (T)		$B_z(P_2)$ (T)	
	sim.	meas.	sim.	meas.
1000	0.32	0.36	0.24	0.24
3000	0.84	0.84	0.58	0.63
4500	0.98	0.99	0.66	0.72
5000	1.02	1.03	0.70	0.74

TABLE VI
Magnetic force f_z acting at the center pole

$\Theta(A)$	F_z (N)	
	simulation	measurement
1000	7.83	8.1
3000	53.7	54.4
4500	73.2	75.0
5000	77.5	80.1

VII. Iron cored choke

Figure 11 shows the principal setup of the second verification example. A choke consisting of laminated iron with a high and constant permeability and a small region with laminated nonlinear iron is coupled to an electric network. If the network is excited by a voltage pulse

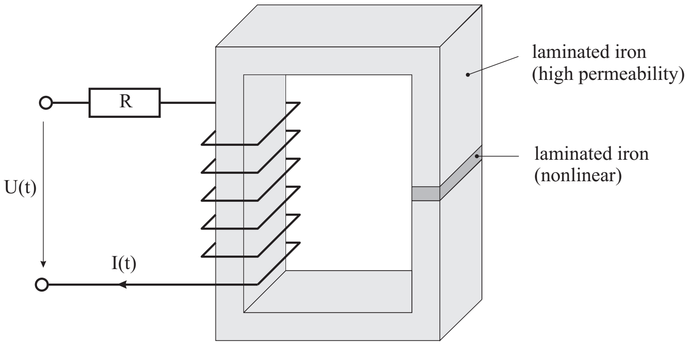

Fig. 11. Principal setup of the voltage clamped nonlinear iron choke

$$U(t) = \hat{U} e^{-\frac{t}{\tau}}, \tag{116}$$

an electric current $I(t)$ and a magnetic flux $\Phi(t)$ are generated, which will be computed with the developed multigrid tool and for verification with a network model.

A. Network model

In order to derive a network model of the nonlinear example, first the magnetic stray field in the air filled space outside the choke is neglected. This is possible, because the linear part of the choke has a very high permeability, and the gap in this part, which is filled with nonlinear iron, is very small compared to the other dimensions of the choke. Additionally, a homogeneous distribution of the magnetic flux in the rectangular cross section of the choke is assumed. Using these conditions the problem can

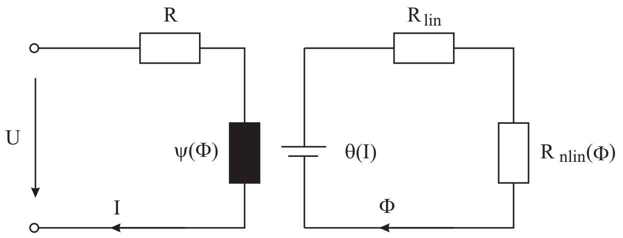

Fig. 12. Coupled electrical-magnetical network

be expressed by the nonlinear coupled network displayed in Fig. 12. Here, Ψ denotes the interlinkage flux, θ the excitation of the magnetic circuit,

$$R_{lin} = \frac{l_{lin}}{\mu_{lin} A} \tag{117}$$

the magnetic resistance of the linear part of the choke and

$$R_{nlin}(\Phi) = \frac{l_{nlin}}{\mu_{nlin}(\Phi) A} \tag{118}$$

the magnetic resistance of the nonlinear part of the choke. l_{lin} and μ_{lin} denote the length and the permeability of the linear resistor, l_{lin} and μ_{lin} the length and the permeability of the nonlinear resistor and, A the constant area of the cross section of the choke.
Using the developed network model the transient behavior of the nonlinear choke is described by the equations

$$\theta = R_{lin}\Phi + R_{nlin}(\Phi)\Phi \tag{119}$$

$$U = RI + N\frac{\partial \Phi}{\partial t}, \tag{120}$$

where $N = \Theta/I$ denotes the number of turns of the excitation coil. In order to find an analytical solution of the coupled equations (119) and (120) the simple dependency

$$\mu_{nlin} = \mu_0 \frac{\mu_s}{1 + kB} \tag{121}$$

between the induction $B = \Phi/A$ and the nonlinear permeability is assumed. Thereby, μ_0 denotes the permeability in vacuum, μ_s the relative initial permeability and k the strength of the nonlinearity. Using (117) - (121), the nonlinear differential equation

$$\frac{R}{N\mu_0}\left(\frac{l_{lin}}{\mu_{lin}} + \frac{l_{nlin}}{\mu_s}\right) B + \frac{R l_{nlin} k}{N\mu_0\mu_s} B^2 + NA\frac{\partial B}{\partial t} = U(t) \tag{122}$$

can be derived. Equation (122) is of the Riccati type [24], which can be solved for special cases of excitations $U(t)$.

In the case of the exponential decreasing excitation (116) the solution of (122) is

$$B(t) = \frac{\sqrt{-\frac{R l_{nlin} k \hat{U}}{N\mu_0\mu_s}}\,(J(\xi,\zeta)Y(\xi,\eta) - J(\xi,\eta)Y(\xi,\zeta))}{\sqrt{e^{t/\tau}\frac{R l_{nlin} k}{N\mu_0\mu_s}}\,(J(\chi,\xi)Y(\xi,\zeta) - J(\xi,\zeta)Y(\xi,\zeta))}, \tag{123}$$

where the abbreviations

$$\xi = 1 - \frac{R\tau(l_{nlin}\mu_{lin} + l_{lin}\mu_s)}{N^2 A\mu_0\mu_S\mu_{lin}}, \tag{124}$$

$$\zeta = -\frac{2\tau}{NA}\sqrt{-\frac{R l_{nlin} k\hat{U}}{N\mu_0\mu_s}}, \tag{125}$$

$$\eta = e^{-t/\tau}\zeta \quad \text{and} \tag{126}$$

$$\chi = -\frac{R\tau(l_{nlin}\mu_{lin} + l_{lin}\mu_s)}{N^2 A\mu_0\mu_s\mu_{lin}} \tag{127}$$

are used. J(m,n) and Y(m,n) are the Bessel and Weber functions of the m-th kind with the argument n [25]. If $B(t)$ is known the electric current I can be easily found by reformulating (119).

B. Numerical simulation

The transient behavior of the nonlinear iron cored choke was now computed by the above presented simulation technique. The 3D numerical model consisted of 40000 edges and was calculated for 300 timesteps. The properties of this example are displayed in Table VII. In Fig. 13 the transient induction $B(t)$, as obtained by the numerical simulation, is compared with the analytical simulation. Thereby, an excellent agreement can be detected. For comparison, the induction $B(t)$ is also displayed for the linear model ($k = 0$), which is much higher because it is not limited by the nonlinear behavior of the material. Fig. 14 compares the electric current of the numerical computation and the analytical solution. Also in this case an excellent agreement can be observed. In the nonlinear case the excitation causes a strong magnetic saturation which decreases the inductivity of the choke. Therefore, the slew rate of the current I is for the nonlinear case much higher than for the linear computation.

TABLE VII
Properties of the iron cored choke

$l_{lin} =$	$560\ mm$	$k =$	30
$l_{nlin} =$	$1\ mm$	$N =$	10
$A =$	$100\ mm^2$	$R =$	$100\ \Omega$
$\mu_0 =$	$4\pi\,10^{-7}\ Vs/Am$	$\hat{U} =$	$100\ V$
$\mu_{lin} =$	10^5	$\tau =$	$0.1\ ms$
$\mu_s =$	10^4		

VIII. Magnetically excited aluminum plate

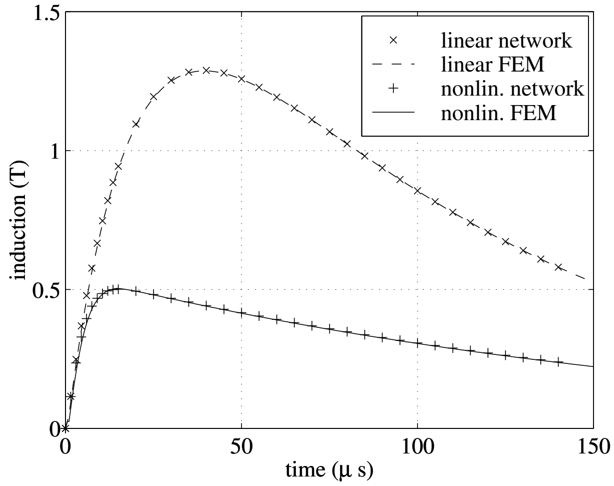

Fig. 13. Induction in the center of the cross section of the choke

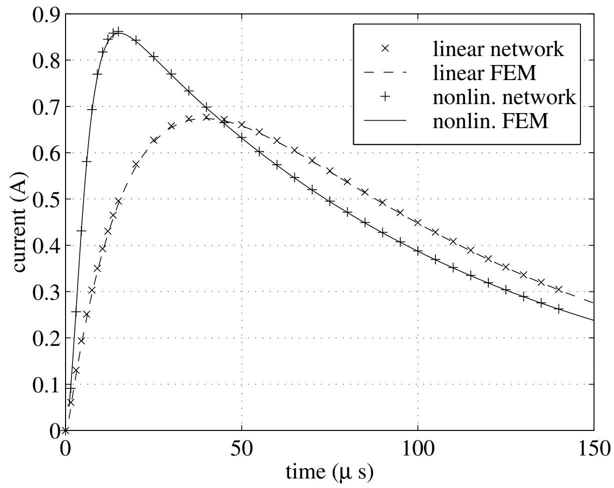

Fig. 14. Current in the coil of the iron cored choke

To demonstrate the simulation of coupled magneto-mechanical systems, the structure in Fig. 15 is considered. It consists of a 3 mm thick aluminum plate, which is clamped at two sides. The used material properties are $E_{Alu} = 7.5 \times 10^{10} Nm/m^2$, $\nu_{Alu} = 0.337$, $\rho_{Alu} = 2.7 \times 10^3 kg/m^3$ and $\gamma_{Alu} = 35 \times 10^6\, 1/\Omega m$. At a distance of 3.5 mm a copper coil with 145 turns and a resistance of $R = 1.35\,\Omega$ is situated among the plate. If a transient electric current I flows in the coil, a magnetic field is produced, which induces eddy currents in the aluminum plate. The Lorentz force (19) resulting thereof generates a mechanical displacement $\vec{d}$, which additionally influences the behavior of the plate by electromotive forces. Since in this case the Péclet-number (14)

$$Pe = \frac{\mu\gamma v h}{2} \ll 1$$

is small, this electromotive force is negligible. Another

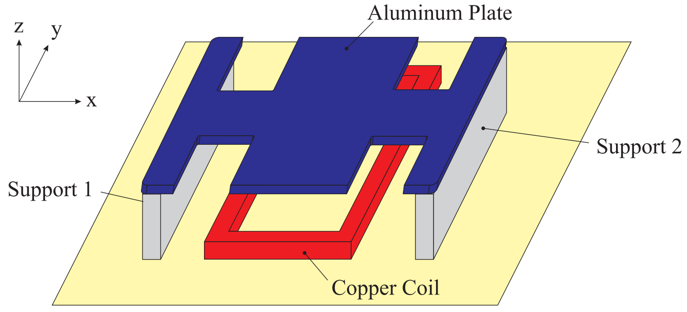

Fig. 15. Principal setup of the magnetically excited aluminum plate

coupling effect between the magnetic and the mechanical field are geometric nonlinearities, i.e. the strong deformation of the plate causes a variation of the magnetic field. In order to achieve a strong excitation of the plate, the coil is loaded by a capacitor discharge, where the resulting current impulse is shown in Fig. 16. The relevant

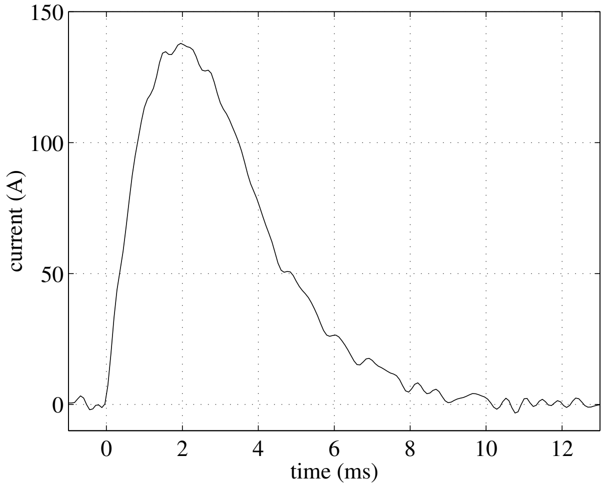

Fig. 16. Current pulse in the coil among the aluminum plate

frequencies of this impulse are lower than $f = 1000$ Hz. Therefore, the minimal penetration depth

$$\delta = \frac{1}{\sqrt{\pi\mu_{Alu}\gamma_{Alu} f}} \qquad (128)$$

of the magnetic field in the aluminum plate is 2.69 mm [23]. Since the thickness h of the plate is in the same order of magnitude, a discretization of h with 8 linear edge tetrahedron elements is sufficient.

In the considered frequency domain only global oscillations of the aluminum plate appear and, hence, a coarse discretization of the mechanical problem with 4 linear nodal tetrahedron elements in h is adequate. Thereby, the following FE meshes results:

- Magnetic problem:
  407530 linear edge tetrahedron elements, 356587 edges (DOFs)

- Mechanical problem:
  68241 linear nodal tetrahedron elements, 25580 nodal DOFs

Although only the aluminum plate is moving, the mechanical problem is solved at the whole domain. The air filled space is considered with a very low Young's modulus E. By taking into account the whole domain in the mechanical simulation, the large displacements in the plate are transfered to the air, and therefore inadmissible distortions or interpenetration of the finite elements are avoided. In Fig. 17 a cross-section of the 3D simulation model with the applied boundary conditions is displayed. In the model the symmetry in the x-z and y-z plane is exploited. The coupling technique, which was presented

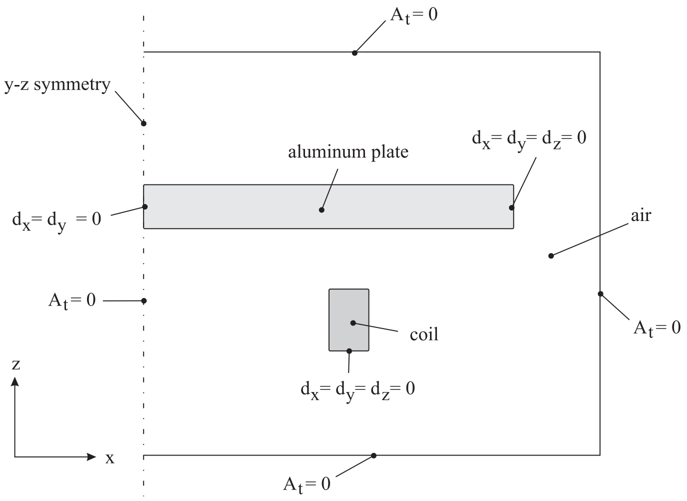

Fig. 17. Cross-section of the 3D model in the x-z plane

in section IV. is now applied to this problem. The time step width is chosen as

$$\Delta t = \frac{1}{20 f_{max}} = 50\,\mu s. \tag{129}$$

Therewith, 400 time steps are necessary for a requested simulation time of 20 ms.

A. Simulation times

1) MG techniques: The simulations are performed on a SGI ORIGIN with a 300 MHz RS12000 processor. Using the chosen time step width Δt, only one iteration loop of the iterative method presented in section IV. is necessary. The solution time consists of the following main parts:

- Solution of the matrix equation system (58) by using the magnetic edge element mesh
  8 MG-PCCG iterations, 95 s
- Solution of the matrix equation system (63) by using the mechanical nodal element mesh
  18 MG-PCCG iterations, 19 s
- Assembling of matrices and right hand sides, calculation of magnetic flux etc. 12.26 s

Therewith, the whole calculation time for one time step is 126.25 seconds, and for all 400 time step the accumulated time is 14 hours.

2) Calculation with a conventional approach: Using a conventional simulation technique the magnetic field as well as the mechanical field are solved at the same FE mesh. Since the magnetic field demands a relatively fine grid the following discretizations arise:

- Magnetic problem:
  407530 linear edge tetrahedron elements, 356587 edges (DOFs)
- Mechanical problem:
  407530 linear nodal tetrahedron elements, 204741 nodal DOFs

Therefore, the magnetic field has exactly the same number of DOFs as using the MG method, but the mechanical problem has much more DOFs compared to MG. The solution of the matrix equation system is performed by the CG method with adapted block-preconditioning (PCCG), but without MG cycle. Using this solvers the following solution times arise:

- Solution of the matrix equation system (58) by using the common FE mesh
  67 PCCG iterations, 489 s
- Solution of the matrix equation system (63) by using the common FE mesh
  32 PCCG iterations, 712 s
- Assembling of matrices and right hand sides, calculation of the magnetic flux etc.
  35 s

Therewith, the simulation process needs an accumulated simulation time of 137 hours for all 400 time steps, i.e. the solution time of the conventional approach is 9.8 times higher, than using the MG method.

B. Comparison measurement - simulation

In order to verify the developed scheme, simulated results were compared to measurements. The measured and simulated displacement d_z, in the center of the plate is displayed in Fig. 18. Thereby, a good agreement between measurement and geometrically nonlinear simulation can be detected. The same example was calculated with a geometrically linear approach, i.e. the magnetic problem is solved at the undeformed geometry. In Fig. 19 the displacement d_z obtained by this linear method is compared to the measurements. Thereby, not such a good agreement is observed. To analyze this situation in more

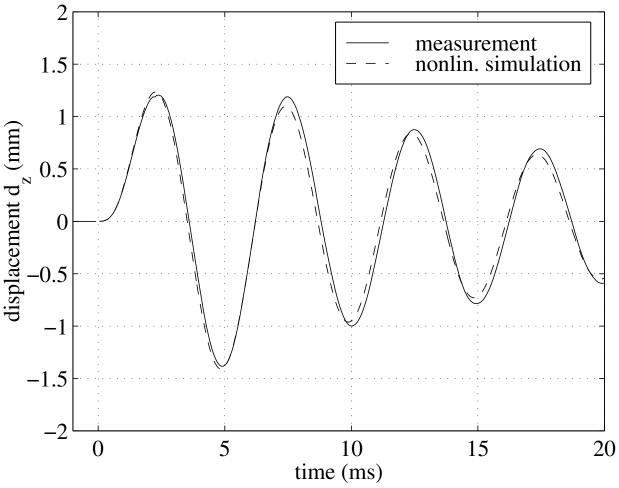

Fig. 18. Displacement d_z in the center of the aluminum plate

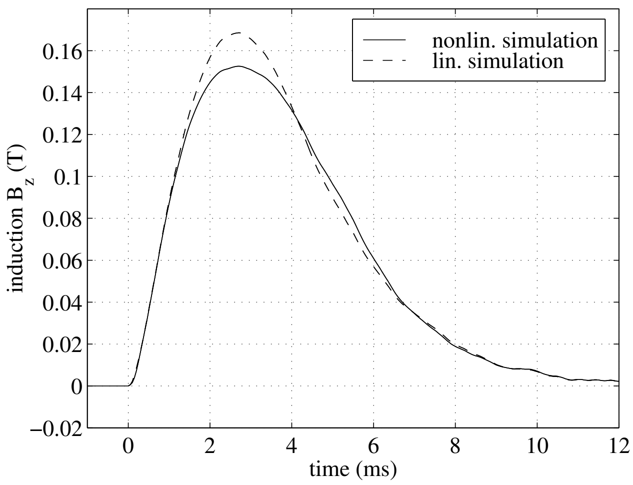

Fig. 20. Magnetic induction B_z in the center of the plate

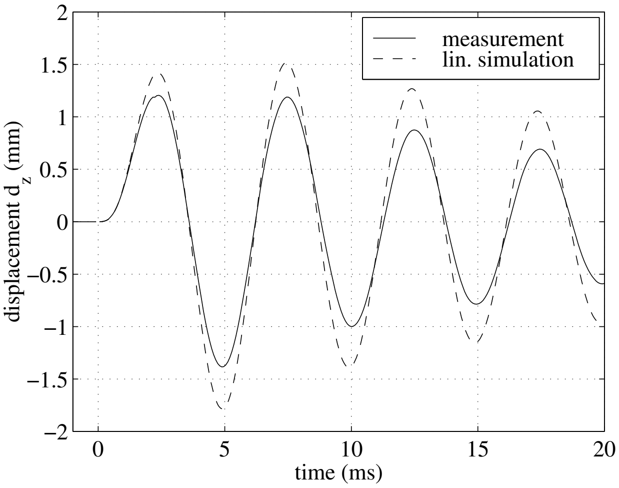

Fig. 19. Displacement d_z in the center of the aluminum plate

detail the simulated inductions B_z in the center of the plate are displayed in Fig. 20. After loading the coil with the current pulse the plate moves away from the coil and increases the air gap. Since the maximal value of the displacement d_z is not small in comparison to the air gap between the plate and the coil, the induction in the plate is smaller than without deformation. Therefore, the linear simulation results in Fig. 20, which does not take into account this deformation, shows a too large induction B_z.

IX. Conclusion

A new simulation technique for the numerical calculation of 3D magneto-mechanical systems which takes into account all coupling effects between the mechanical and magnetic field has been presented. Thereby, the application of a hierarchy of FE meshes enables a much faster simulation of transient and large scaled 3D problem than conventional approaches.
The matrix equation systems for the mechanical and the magnetic system which arising in the iterative calculation scheme, are solved by fast multigrid solution techniques. Thereby, the properties of the mechanical discretization (3D nodal elements) and the magnetic discretization (3D edge elements) are analyzed in detail, and suitable multigrid components (Prolongation, Restriction, Smoothing) for the above problems are derived.
A considerable reduction of the necessary degrees of freedom is achieved by applying different discretizations for the mechanical and magnet mesh. Thereby, the application of grid-transfer-operators enables the data transfer between the mechanical and magnetic mesh.
The validity of the presented multigrid simulation scheme and it's advantages with respect to the necessary simulation time have been confirmed by three different verification examples.

References

[1] E. Vassent, G. Meuner, A. Foggia, and R. Reyne, "Simulation of induction machine operation using a step by step finite element method coupled with circuits and mechanical equations," *IEEE Transactions on Magnetics*, vol. 37, no. 6, pp. 5232–5234, November 1991.

[2] Y. Kawase, O. Miyatani, and T. Yamaguchi, "Numerical analysis of dynamic characteristics of electromagnets using 3-d finite element method with edge elements," *IEEE Transactions on Magnetics*, vol. 30, no. 5, pp. 3248–3251, September 1994.

[3] Z. Ren and A. Razek, "Force calculation by maxwell stress tensor in 3d hybrid finite element - boundary integral formulation," *IEEE Transactions on Magnetics*, vol. 26, no. 5, pp. 2774–2776, September 1990.

[4] S. Kurz, J. Fetzer, and G. Lehner, "Threedimensional transient fem-bem coupled analysis of electrodynamic levitation problems," *IEEE Transactions on Magnetics*, vol. 32, no. 3, pp. 1062–1065, May 1996.

[5] M. Kaltenbacher, H. Landes, and R. Lerch, "An Efficient Calculation Scheme for the Numerical Simulation of Coupled Magnetomechanical Systems," *IEEE Transactions on Magnetics*, vol. 33, no. 2, pp. 1646–1649, March 1997.
[6] M. Jung and U. Langer, "Applications of multilevel methods to practical problems," *Surv. Math. Ind.*, vol. 1, pp. 217–257, 1991.
[7] F. Ziegler, *Mechanics of Solids and Fluids*, Springer-Verlag, Vienna, 1 edition, 1991.
[8] S. Kurz, J. Fetzer, G. Lehner, and W. Rucker, "A novel formulation for 3d eddy current problems with moving bodies using a lagrangian description and bem-fem coupling," *IEEE Transactions on Magnetics*, vol. 34, no. 5, pp. 3068–3073, September 1998.
[9] T.J.R. Hughes, *The Finite Element Method*, PRENTICE-HALL, New Jersey, 1 edition, 1987.
[10] K.J. Bathe, *Finite Element Procedures*, PRENTICE-HALL, New Jersey, 1996.
[11] O. Biró, K. Preis, and K.R. Richter, "On the Use of the Magnetic Vector Potential in the Nodal and Edge Finite Element Analysis of 3D Magnetostatic Problems," *IEEE Transactions on Magnetics*, vol. 32, no. 3, pp. 651–654, May 1996.
[12] J. Nédélec, "Mixed finite elements in R^3," *Numer.Math.*, pp. 315–341, 1980.
[13] Z. Ren and A. Razek, "A Strong Coupled Model for Analysing Dynamic Behaviours of Non-linear Electromagnetic Systems," *IEEE Transactions on Magnetics*, vol. 30, no. 5, pp. 3252–3255, September 1994.
[14] P.S. Silvester and R.L. Ferrari, *Finite elements for electrical engineers*, Cambridge University Press, 3 edition, 1996.
[15] A. Brandt, "Guide to multigrid developement," in *Proceedings of Conference on Multigrid Methods*, 1981, pp. 220–312.
[16] H.R. Schwartz, *Numerische Mathematik*, B.G. Teubner, Stuttgart, 1 edition, 1993.
[17] O. Axelsson, *Iterative Solution Methods*, Cambridge University Press, 2 edition, 1996.
[18] R. Hiptmair, "Multigrid method for Maxwell's equations," *SIAM J. Numer. Anal.*, vol. 36, no. 1, pp. 204–225, May 1996.
[19] D.N. Arnold, R.S. Falk, and R. Winther, "Multigrid in H(div) and H(curl)," 1998, Department of Mathematics, Penn State University.
[20] N. Takahashi, T. Nakata, and H. Morishige, "Summary of results for problem 20 (3-d static force problem)," *COMPEL*, vol. 14, no. 2/3, pp. 57–75, 1995.
[21] B. Heise, "Mehrgitter-Newton-Verfahren zur Berechnung nichtlinearer magnetischer Felder," Disseration, TU Chemnitz, 1994.
[22] K. Fujiwara, T. Nakata, and H. Ohashi, "Improvement fo convergence characteristic of iccg method for the a-ϕ method using edge elements," *IEEE Transactions on Magnetics*, vol. 32, no. 3, pp. 804–807, May 1996.
[23] E. Philippow, *Grundlagen der Elektrotechnik*, Hütig Verlag, Heidelberg, 8 edition, 1989.
[24] K. Meyberg and P. Vachenauer, *Höhere Mathematik 2*, Springer, Berlin, 1 edition, 1991.
[25] I. Bronstein and K. Semendjajew, *Taschenbuch der Mathematik*, Teubner, Leipzig, 25 edition, 1991.